JACS
JOURNAL OF THE AMERICAN CHEMICAL SOCIETY

Communication

pubs.acs.org/JACS

Real-Time Observation of Crystal Evaporation in a Metal Phosphate at High Temperature

Sung-Yoon Chung,*[,†,‡] Young-Min Kim,[§] Si-Young Choi,[∥] and Jin-Gyu Kim[§]

[†]Graduate School of EEWS and KAIST Institute for the Nanocentury, Korea Advanced Institute of Science and Technology (KAIST), Daejeon 305-701, Korea

[‡]Nalphates LLC, Wilmington, Delaware 19801, United States

[§]Korea Basic Science Institute, Daejeon 305-333, Korea

[∥]Korea Institute of Materials Science, Changwon 641-831, Korea

Supporting Information

ABSTRACT: A number of experimental studies on crystal growth have been performed in connection with a variety of crystalline systems ranging from simple oxides to complex organic compounds. In contrast, little is known regarding how crystals evaporate. By using a combination of real-time high-resolution electron microscopy at high temperature, image simulations, and density functional theory calculations, we demonstrate the evaporation of metal-phosphate nanocrystals with flat surfaces at atomic resolution. In situ imaging and direct comparison with image simulation results reveal that, while a layer-by-layer lateral process is macroscopically maintained, the cations preferentially evaporate over the $(PO_4)^{3-}$ tetrahedral anions from shrinking ledges. The present observations provide the first atomic-scale experimental details of the evaporation of complex oxides, emphasizing the value of direct visualization in real time.

Observation and appropriate control of growth and dissolution/evaporation behavior of crystals during the Ostwald ripening process have been recognized as important issues in crystallization studies over the past several decades.[1,2] In addition to well-known classical theories for two-dimensional nucleation and layer growth (the Gibbs−Volmer theory)[3] and dislocation-assisted spiral growth (the Burton−Cabrera−Frank theory),[4] a number of experimental results showing peculiar crystal growth characteristics in many crystalline systems have been reported.[5] Furthermore, recent progress in imaging techniques has enabled nanoscale demonstration of growth mechanisms in various materials, encompassing proteins, Zn-insulin, and complex zeolites as well as simple alloys and oxides.[6]

In contrast to the very broad spectrum of studies on crystal growth, the majority of works concerning crystal dissolution have been associated with glasses and minerals in relation to geochemical and weathering research.[7−9] The formation of ledges and etch pits on quartz[7] and the presence of a Si- and H-rich amorphous layer on silicates minerals[8] are examples of important features during crystal dissolution. Most of these previous studies, however, are restricted to crystals that dissolve into an aqueous solution and subsequent surface analyses with scanning probe microscopy. Despite that a variety of crystalline particles are obtained via a solid-state reaction without association of solution phases, there has been a significant lack of investigations regarding how crystals evaporate.

In the present work, we selected an olivine-type metal phosphate, $LiFePO_4$, as a model system from the many complex oxyanion crystals that are of scientific importance. As in carbonate and silicate groups, the phosphate $[PO_4]^{3-}$ tetrahedra provide a stable framework in the crystal structure due to the high degree of covalency between P and O.[10] Therefore, the growth and evaporation of $LiFePO_4$ can be observed without concern of structural instability by oxygen evolution in the high vacuum condition of a transmission electron microscope.[11] Using *in situ* high-resolution electron microscopy (HREM) with a heating specimen holder, in this study we demonstrate the atomic-level evaporation behavior of quaternary phosphate crystals in real time at high temperature. Systematic image simulations based on the multislice method and density functional theory (DFT) calculations using the CASTEP code were also performed to identify the dynamic variation of atomic configurations and the resulting charge redistribution in the surface region during evaporation (see the Supporting Information for experimental details). Note that the term, 'evaporation', in this Communication is used as the counter process to 'crystal growth' rather than simple vaporization of materials at elevated temperature.

When we observed evaporating planar surfaces in real time, their evaporation appeared to occur basically through a reverse process of the lateral growth. As exemplified in Figure 1, lateral step evaporation could be readily observed at the flat surfaces in $LiFePO_4$. To closely monitor the step evaporation at an atomic level, shrinking nanocrystals were observed in a proper projection where the unit of evaporation slices could be sufficiently resolved in transmission electron microscopy (TEM). Figure 2a shows a [122]-projection HREM image for a surface region of a shrinking $LiFePO_4$ crystal at 600 °C. The fast Fourier transform (FFT) of the image indicates that the flat surface is the $(\bar{2}10)$ plane. From the image simulation along with the schematic illustration of the atomic array, the center of the strong black contrast in the real HREM image

Received: February 18, 2013
Published: May 20, 2013

   dx.doi.org/10.1021/ja401753u | *J. Am. Chem. Soc.* 2013, 135, 7811−7814

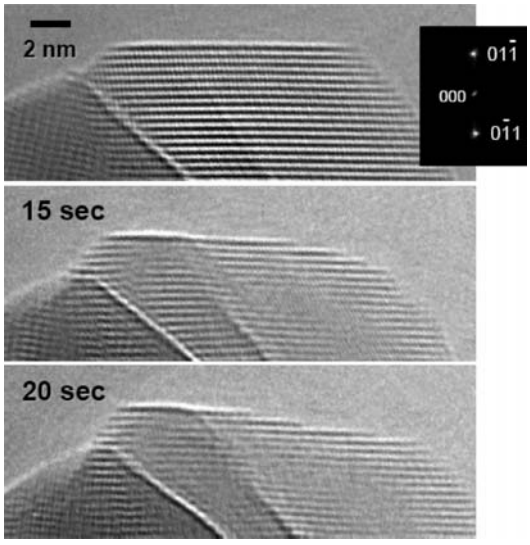

Figure 1. A series of *in situ* HREM images of shrinking $LiFePO_4$ crystals. A laterally evaporating behavior is verified in real time on the flat surface.

corresponds to a Li column in this projection (see the enlarged image). As previously revealed in Figure 1, slice-by-slice step evaporation in this crystal is consistently demonstrated in the series of *in situ* HREM images shown in Figure 2b–d. It is observable that the top slice (yellow) eventually disappears (Figure 2d) and the subsequent second and third slices (blue and red) also gradually reduce in width. A subsequent series of *in situ* HREM images is also provided in Figure 3, showing that each slice (blue, red, and green) consecutively evaporates in an identical manner.

If the ledges of evaporating slices in the HREM images are scrutinized, noteworthy variation of atomic-scale lattice fringes can be found. The enlargements in the right column in Figure 3 are magnified lattice images for each region denoted by a yellow rectangle in the left column. While the periodic lattice fringes are well maintained over the bulk region, uneven image features with broken periodicity are frequently observed around the ledges of shrinking steps, as indicated by an arrow in each enlargement. This irregular appearance of the black contrast in the images can be categorized into three different types: one that lies between the periodic rows of black fringes (Figure 3a,b), another with much less black in contrast (Figure 3c), and the other at lower positions in the same row (Figure 3d).

A high-resolution lattice image in bright-field TEM is a phase-contrast image, the intensity variation of which stems from the phase change of diffracted electron waves traveling through the projected atomic potentials of a thin specimen.[12] Therefore, the local changes in lattice fringes that are observed in the magnified HREM images of Figure 3 are expected to result from the variation of the atomic configuration around the ledges during evaporation. To identify such configurational variation at an atomic level, HREM image simulations were utilized for direct comparison with the experimentally obtained images. Figure 4a shows the simulation result (middle) when the ledge consists of four stoichiometric $[LiFePO_4]$ units, as indicated by a white circle in the schematic of an atomic array (left). A real-time HREM image corresponding with the simulated image is also provided in the right column, showing the periodic arrangement of the contrast features over all slice layers (yellow, red, blue, and green). Note that the slight

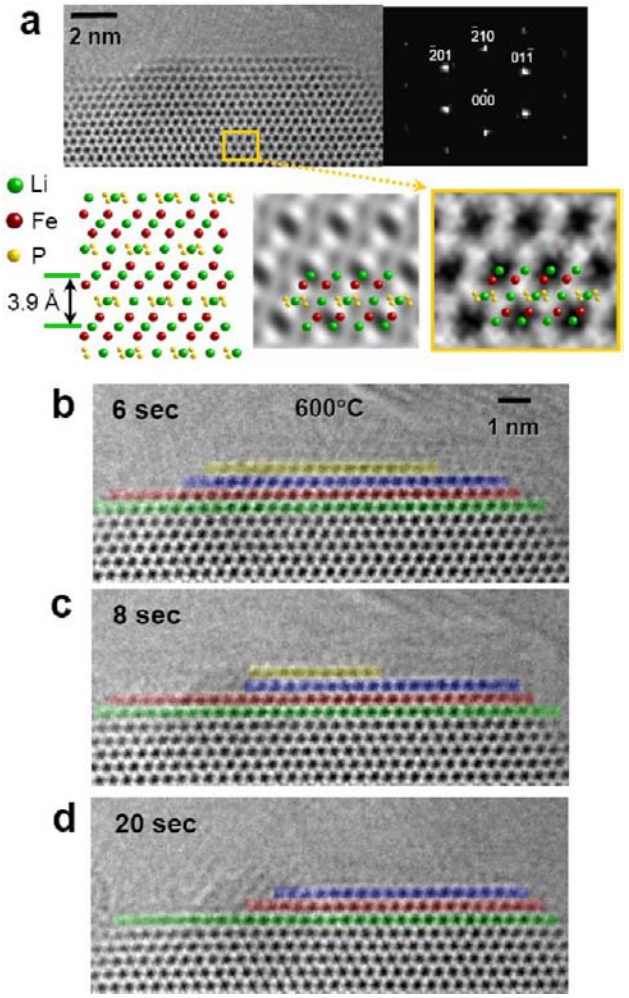

Figure 2. *In situ* HREM images of a shrinking $LiFePO_4$ crystal at 600 °C. (a) The HREM image and its FFT of a crystal in the [122] projection are shown, indicating that the surface is parallel to a $(\bar{2}10)$ plane. Image simulation (middle) was also carried out to find the best matching in lattice fringes with the HREM image (right) (t = 9 nm and Δf = +14 nm). (b–d) Consistently in Figure 1, this series of *in situ* HREM images for the surface region shows that the evaporation takes place via a layer-by-layer lateral process. Each slice layer is discriminated in colors. The complete elimination of the yellow slice is finally observed in (d).

difference in detailed lattice fringes between experimentally obtained and simulated images is recognized because the Debye–Waller factors for thermal scattering at 600 °C were not considered during image simulations.

Three appropriate assumptions were made for the specific HREM image simulation during evaporation. First, $[PO_4]$ was treated as an anion without separation, based on the strong covalency between P and O, as aforementioned. In fact, our *ab initio* molecular dynamic (MD) simulation has confirmed that the P–O bond in $LiFePO_4$ does not break even in a liquid phase at 2000 K, maintaining the $[PO_4]^{3-}$ tetrahedra (see Figure S1). Second, it is virtually impossible to discriminate whether Li is present at the ledges from HREM images, because very light elements such as Li make a negligible contribution to image contrast in TEM. Therefore, we did not deal with the two cations, Li and Fe, individually, but instead assumed that their evaporation would take place together at the same time for simplicity. Last, substantial atomic reconstruction

dx.doi.org/10.1021/ja401753u | *J. Am. Chem. Soc.* 2013, 135, 7811–7814

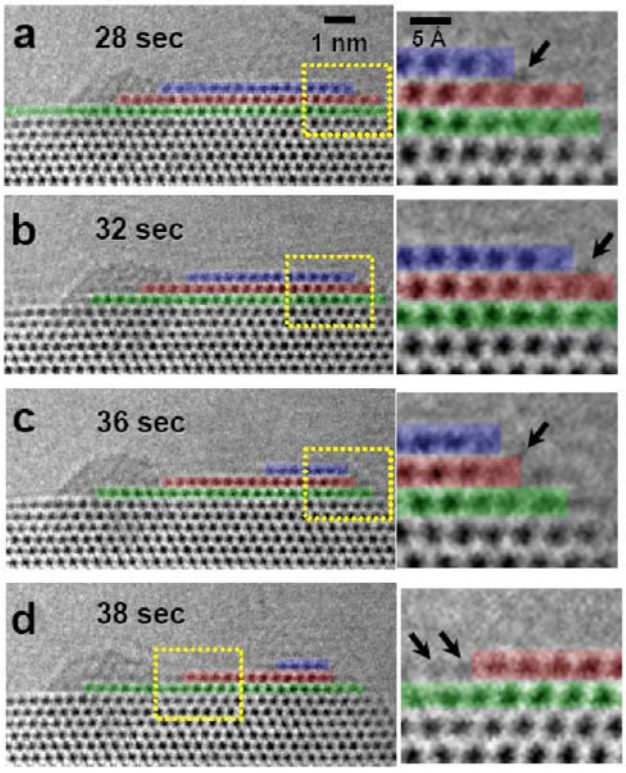

Figure 3. Further series of *in situ* HREM images in the surface region. (a–d) The consecutive evaporation of each slice layer (blue, red, and green) with time is confirmed. Magnified images for the ledge regions denoted by yellow rectangles are given in the right column. As indicated by arrows, the black contrast features that deviate from the periodic bulk lattice fringes can be identified, implying dynamic variation in the atomic configuration at the ledges during evaporation.

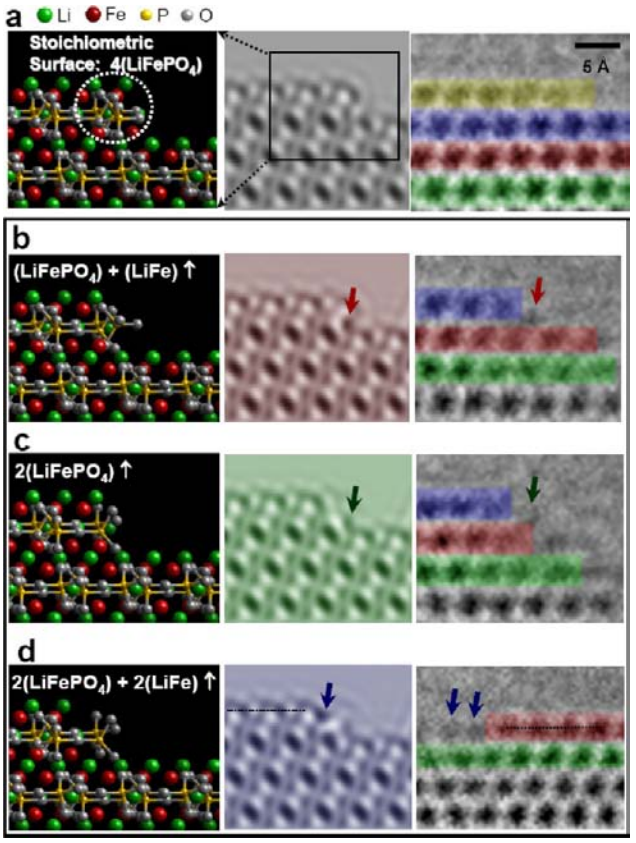

Figure 4. Comparison between simulated and experimental *in situ* HREM images of an evaporating ledge. (a) The simulation result (middle) shows good agreement with the corresponding HREM image (right) when a ledge consists of four stoichiometric $[LiFePO_4]$ units, as illustrated schematically (left). (b–d) Each represents the evaporation of $[LiFePO_4 + LiFe]$ (b), two $[LiFePO_4]$ (c), and two $[LiFePO_4 + LiFe]$ (d) out of four $[LiFePO_4]$ units, revealing that the simulated images match well with corresponding HREM images. The appearance of the irregular black contrast resulting from the variation of atomic configuration at the ledge is indicated by red, green, and blue arrows, respectively. A black broken line is drawn to indicate the down shift of the black image contrast denoted by blue arrows in (d).

that can be observed at a thermodynamically equilibrium state were also assumed not to occur at the evaporating terraces and ledges.

A series of image simulations and a comparison with experimentally obtained HREM images conclusively revealed that the local stoichiometry at the ledge was not maintained during evaporation. Figure 4b shows the image simulation on the middle column when $[LiFePO_4 + LiFe]$ is evaporated from the initial four $[LiFePO_4]$ units at the ledge, resulting in cation-deficient (or $[PO_4]^{3-}$ anion-excess) nonstoichiometry. As indicated by a red arrow, the black image contrast that cannot be constructed in the bulk lattice clearly appears between the layers. The real HREM images in the right column show good agreement with these simulated images as well, clearly supporting the occurrence of the nonstoichiometry at the edge. Another plausible case is illustrated in Figure 4c where two $[LiFePO_4]$ units are evaporated. Compared with the appearance of strong black contrast (red arrow) shown in Figure 4b, however, the change in image features between the layers in Figure 4c is not considerably substantial, as denoted by a green arrow in both the simulation and the corresponding image. Figure 4d presents the other cation-deficient configuration by evaporation of two $[LiFePO_4 + LiFe]$ units from the ledge. The irregular black image contrast in this simulated image is placed in the same layer with a slight down shift (blue arrow). The two black fringes at a ledge indicated by blue arrows in the consistent HREM image are thus determined to result from the cation-deficient dynamic situation. An additional image simulation result for the anion-deficient case is provided in the Figure S2, demonstrating that this is not compatible with the experimentally obtained HREM images.

A notable feature in this study is that the atomic configuration at ledge regions can vary dynamically during the evaporation process even if crystals with flat surfaces evaporate through a slice-by-slice lateral mechanism from a macroscopic perspective. In particular, the frequent appearance of cation-deficient ledges directly indicates that Li and Fe preferentially evaporate over the $[PO_4]^{3-}$ anions. Figure 5a depicts the preferential evaporation of Li and Fe (white arrows) at the ledge in the [001] projection. From our DFT calculations, significant increments in the Mulliken charge were identified for the neighboring Fe and O of the evaporating Li and Fe. As indicated in Figure 5b, for example, "$Fe_{(1)}$" in orange and "$O_{(1)}$" and "$O_{(2)}$" in light blue, which are the Fe and O atoms closest to the evaporated Fe, reveal a large positive change of the charge (+1.06e → +1.16e in $Fe_{(1)}$; −0.98e → −0.78e in $O_{(1)}$; −1.04e → −0.92e in $O_{(2)}$), while no considerable variation in the charge (less than 0.04) is found in most other neighbor atoms. Therefore, these calculations show that the nearest-neighboring Fe and O play a key role in

dx.doi.org/10.1021/ja401753u | *J. Am. Chem. Soc.* 2013, 135, 7811–7814

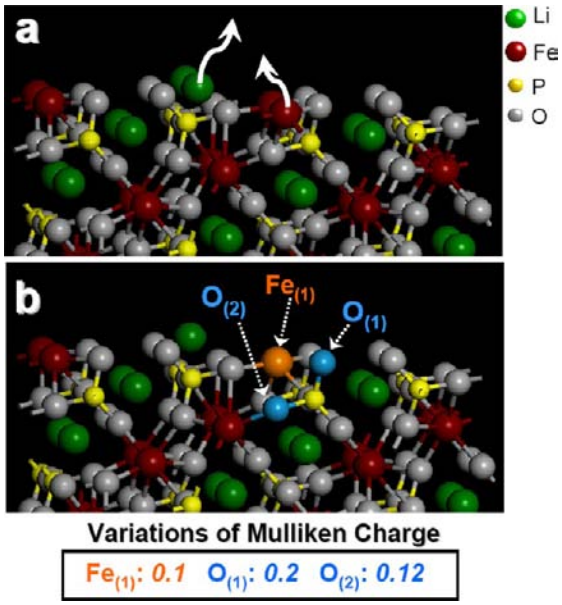

Figure 5. (a) Relaxed $(\bar{2}10)$ surface structure in the vicinal [001] projection. The Li and Fe that are about to evaporate are denoted by white arrows. (b) Variations of the Mulliken charge of the neighboring atoms after evaporation. $Fe_{(1)}$ in orange and $O_{(1)}$ and $O_{(2)}$ in light blue are, respectively, the nearest-neighboring iron and oxygen atoms of the evaporated Fe. They exhibit a substantial increment in their charge values, whereas the variations of Li and P are marginal.

the rapid charge transfer to evaporating cations as efficient electron donors during the evaporation process. The details of the Mulliken charge variations of other neighbor atoms including Li and P are provided in Figure S3.

Crystal dissolution in a variety of carbonates, silicates, and sulfates having an oxyanion framework ($[CO_3]^{2-}$, $[SiO_4]^{4-}$, and $[SO_4]^{2-}$, respectively) analogous to that of phosphates also has been studied owing to the related wide range of interest in demineralization and geochemical corrosion.[7−9] Although dealing with simulations in $BaSO_4$, a very recent report based on metadynamics and reactive flux calculations consistently showed preferential detachment of Ba from a stepped surface into an aqueous solution along with the occurrence of intermediate states during dissolution.[13] Extensive real-time investigations and specific comparisons between four different oxyanion-based crystals are thus strongly suggested as future works to understand and control their evaporation/dissolution aspect at high temperature.

In summary, we have directly observed evaporation behavior at flat surfaces of $LiFePO_4$ nanocrystals with atomic resolution at high temperature during Ostwald ripening. While lateral evaporation, which appears to be simply a reverse process of Volmer-type lateral growth, was macroscopically observed on planar terraces of crystals, the dynamic variation of atomic-scale lattice fringes in HREM images could be identified in shrinking ledges. A systematic comparison with image simulations along with DFT calculations demonstrated that the cations evaporate preferentially over the $[PO_4]^{3-}$ oxyanions, accompanying fast charge transfer from the nearest-neighboring Fe and O. Our direct observations thus provide atomic-level visualization of the evaporation aspect in real time in complex oxides, indicating that our combined technique based on high-temperature HREM and systematic image simulations is a powerful tool to understand the dynamic characteristics of crystal evaporation.

■ ASSOCIATED CONTENT

Supporting Information

Details for experiments, *in situ* HREM, image simulations, and DFT calculations, and an additional MD result. This material is available free of charge via the Internet at http://pubs.acs.org.

■ AUTHOR INFORMATION

Corresponding Author

nalphates@gmail.com

Notes

The authors declare no competing financial interest.

■ ACKNOWLEDGMENTS

This work was supported by the National Research Foundation (NRF) of Korea, grant no. 2012M1A2A2671799. S.-Y.C. was also financially supported by the Priority Research Centers Program of the NRF (no. 2012-048034).

■ REFERENCES

(1) Voorhees, P. W. *J. Stat. Phys.* **1985**, *38*, 231−252.
(2) Chernov, A. A. *Modern Crystallography III: Crystal Growth*; Springer: Berlin, 2011.
(3) Volmer, M. *Kinetik der Phasenbildung*; Steinkopff: Leipzig, 1939.
(4) Burton, W. K.; Cabrera, N.; Frank, F. C. *Philos. Trans. R. Soc., A* **1951**, *243*, 299−358.
(5) (a) Malkin, A. J.; Land, T. A.; Kuznetsov, Y. G.; McPherson, A.; De Yoreo, J. J. *Phys. Rev. Lett.* **1995**, *75*, 2778−2781. (b) Pina, C. M.; Becker, U.; Risthaus, P.; Bosbach, D.; Putnis, A. *Nature* **1998**, *395*, 483−486. (c) Sommerdijk, N. A. J. M.; de With, G. *Chem. Rev.* **2008**, *108*, 4499−4550. (d) Zheng, H. M.; Smith, R. K.; Jun, Y.-W.; Kisielowski, C.; Dahmen, U.; Alivisatos, A. P. *Science* **2009**, *324*, 1309−1312.
(6) (a) Ten Wolde, P. R.; Frenkel, D. *Science* **1997**, *277*, 1975−1978. (b) Georgiou, D. K.; Vekilov, P. G. *Proc. Natl. Acad. Sci. U.S.A.* **2006**, *103*, 1681−1686. (c) Brent, R.; Anderson, M. W. *Angew. Chem., Int. Ed.* **2008**, *47*, 5327−5330.
(7) Gratz, A. J.; Manne, S.; Hansma, P. K. *Science* **1991**, *251*, 1343−1346.
(8) Casey, W. H.; Westrich, H. R.; Banfield, J. F.; Ferruzzi, G.; Arnold, G. W. *Nature* **1993**, *366*, 253−256.
(9) (a) Tang, R.; Nancollas, G. H.; Orme, C. A. *J. Am. Chem. Soc.* **2001**, *123*, 5437−5443. (b) Teng, H. H. *Geochim. Cosmochim. Acta* **2004**, *68*, 253−262. (c) Ohlin, C. A.; Villa, E. M.; Rustad, J. R.; Casey, W. H. *Nat. Mater.* **2010**, *9*, 11−19.
(10) (a) Streltsov, V. A.; Belokoneva, E. L.; Tsirelson, V. G.; Hansen, N. K. *Acta Crystallogr., B* **1993**, *49*, 147−153. (b) Chung, S.-Y.; Bloking, J. T.; Chiang, Y.-M. *Nat. Mater.* **2002**, *1*, 123−128.
(11) (a) Chung, S.-Y.; Kim, Y.-M.; Kim, J.-G.; Kim, Y.-J. *Nat. Phys.* **2009**, *5*, 68−73. (b) Chung, S.-Y.; Kim, Y.-M.; Choi, S.-Y. *Adv. Funct. Mater.* **2010**, *20*, 4219−4232. (c) Chung, S.-Y.; Kim, Y.-M.; Lee, S.; Oh, S. H.; Kim, J.-G.; Choi, S.-Y.; Kim, Y.-J.; Kang, S.-J. L. *Nano Lett.* **2012**, *12*, 3068−3073.
(12) Spence, J. C. H. *High-Resolution Electron Microscopy*, 3rd ed.; Oxford University Press: New York, 2003.
(13) Stack, A. G.; Raiteri, P.; Gale, J. D. *J. Am. Chem. Soc.* **2012**, *134*, 11−14.